RSC Advances

PAPER

View Article Online
View Journal | View Issue

Cite this: *RSC Adv.*, 2021, **11**, 24917

Physical and photocatalytic properties of sprayed Dy doped ZnO thin films under sunlight irradiation for degrading methylene blue†

G. El Fidha,[ab] N. Bitri,[b] F. Chaabouni,[b] S. Acosta,[c] F. Güell,[d] C. Bittencourt,[c] J. Casanova-Chafer[e] and E. Llobet*[e]

Dysprosium-doped zinc oxide (ZnO) thin films have been prepared through spray pyrolysis onto glass substrates. Cross-sections of the deposited thin films were assessed through Scanning Electron Microscopy (SEM), showing thicknesses between 200 and 300 nm. The thin film roughness was evaluated using the obtained images from the Atomic Force Microscope (AFM) micrographs. The crystallographic structure of the samples was analyzed by X-ray diffraction (XRD) revealing polycrystalline thin films. However, the slight shift towards a higher 2θ angle in Dy-doped ZnO films as compared to the pure ones indicates the incorporation of Dy^{3+} into the ZnO crystal lattice. The analysis of the oxidation state *via* X-ray photoelectron spectroscopy (XPS) confirms the incorporation of Dy ions in the ZnO matrix. Besides, UV-Vis-NIR spectrophotometry analysis and photoluminescence (PL) spectroscopy showed that bandgap energy values of ZnO decreased when dysprosium doping increased. Therefore, Dy doped ZnO thin films can be potentially used as a solar-light-driven photocatalyst. Among the different doping yields, the ZnO doped with 6% dysprosium provides the highest degradation rate for methylene blue (MB) under solar irradiation. Specifically, 9% of dye degradation was achieved under sunlight irradiation for 120 minutes.

Received 21st May 2021
Accepted 10th July 2021

DOI: 10.1039/d1ra03967a

rsc.li/rsc-advances

1. Introduction

Population growth and the waste from heavy industry have resulted in increasing problems linked to environmental pollution, such as water pollution. Therefore, this pollution constitutes a key challenge nowadays, requiring much research effort to tackle it. For instance, the use of renewable natural resources has been established as a promising method for the degradation of organic and toxic pollutants in wastewater. In particular, photocatalysis has been revealed as one of the most advanced and effective technologies for eliminating dangerous and non-biodegradable chemicals from the environment.[1] In this regard, titanium dioxide (TiO_2) and zinc oxide (ZnO) are the most widely employed semiconductors because they are inexpensive, abundant and relatively clean photocatalysts for photochemical degradation.[2] Previous reports have demonstrated the superior photocatalytic activity of ZnO as compared to TiO_2 because it absorbs a larger fraction and quanta of the sunlight spectrum than TiO_2. In consequence, ZnO usually exhibits a higher degradation capability of organic pollutants than TiO_2 under solar irradiation.[3,4]

Zinc oxide is an n-type semiconductor belonging to the II–VI group. In its wide variety of forms, it has attracted great attention due to its outstanding chemical and physical properties, including high chemical stability.[5] ZnO is a multi-functional metal oxide semiconductor material with high transparency in the visible region, wide-direct bandgap around 3.3 eV and high excitation energy of 60 eV.[6] These properties are quite favorable for optoelectronic applications, photovoltaic conversion, microelectronics, solar cells, gas sensing, light-emitting diodes (LEDs) and photodetectors.[7–9] ZnO shows potential for developing photocatalytic applications, namely, the decomposition of organic pollutants and harmful dyes in water. Additionally, ZnO gathers the requirements needed for this application since it is stable in nature and presents high electronic mobility.[10]

More noticeably, many research efforts have been directed towards enhancing the photocatalytic efficiency of ZnO, proving that increasing the surface defects of the metal oxide induces a shift of the absorption towards the visible light, which increases the efficiency of pollutant degradation under visible

[a]*Université de Tunis, École Nationale Supérieure d'ingénieurs de Tunis, Avenue Taha Hussein Montfleury, 1008 Tunis, Tunisia*

[b]*Université de Tunis El Manar, Ecole Nationale d'Ingénieurs de Tunis, Laboratoire de Photovoltaïque et Matériaux Semi-conducteurs, 1002 Tunis, Tunisia*

[c]*Chimie des Interactions Plasma-Surface (ChIPS), Research Institute for Materials Science and Engineering, Université de Mons, 7000, Mons, Belgium*

[d]*ENFOCAT-IN2UB, Universitat de Barcelona, C/Martí i Franquès 1, 08028 Barcelona, Spain*

[e]*MINOS, Universitat Rovira i Virgili, Avda. Països Catalans, 26, 43007, Tarragona, Spain. E-mail: eduard.llobet@urv.cat*

† Electronic supplementary information (ESI) available. See DOI: 10.1039/d1ra03967a

light irradiation. Recently, more attention is being directed towards the metal doping of ZnO.[11] In particular, doping with rare-earth (RE) ions has attracted great interest due to their highly conductive, magnetic, electrochemical and luminescent properties, which are based on the electronic transitions occurring within 4f energy shells.[12] It has been shown that rare-earth metal doping effectively shifts the absorption to the visible light region and inhibits the recombination of photo-generated charged species, which are favorable conditions for photocatalysis applications.[13]

In previous studies, several rare-earth ions were used to dope ZnO such as Gd^{3+},[14] Tb^{3+} (ref. 15) or Ce^{3+}.[16] Among RE ions, Dy^{3+} doped ZnO has attracted great interest in photocatalytic applications due to its action as an effective scavenger for electrons in the conduction band of ZnO, slowing the recombination rate of charge carriers. This is translated into an enhancement of the photocatalytic activity of ZnO. In this setting, it was already reported that upon doping of ZnO with Ln ions (where Ln might be La, Eu, Gd, Dy and Ho), a complex formation takes place with the interaction of Lewis base and f-orbitals of Ln^{3+} ions.[17] Thus, Ln^{3+} ions are charged, allowing the concentration of organic pollutants on the ZnO surface. Besides, the use of Dy has been demonstrated as a good candidate for photocatalytic application using the sol–gel method.[18] This is explained by the increasing of OH radicals used in the degradation of dye molecules produced by the involvement of f orbitals in delaying electron–hole pair recombination and energy transfer in the photonic process.

Previous works reported the MB degradation using photocatalysts based on ZnO thin films doped with Sn,[19] Sr,[20] Co,[21] Nb-Al[22] or Nd.[23] The choice of nanomaterials with significant photocatalytic activity is a key parameter,[24,25] especially those water-stable for being considered as a potential option to be employed in commercial applications.[26] However, not limited to the nanomaterials employed, Y. C. Chen and collaborators demonstrated that different nanostructure morphologies show variable photocatalytic activities owing to divergent efficiencies towards dye degradation.[27] Thereby, a wide range of possibilities is available to tune the photocatalytic activity of the sensitive layers.

To the best of our knowledge, MB is one of the dyes present in wastewater from textile industries. MB can cause negative effects on the environment since it prevents sunlight from entering the body of water affecting organisms in the aquatic environment. Ingestion of MB may cause a burning sensation which leads to vomiting and can as well produce eye burnt resulting in permanent injury.[28] Since solar energy is a sustainable energy source, the use of photocatalytic nanomaterials is a promising technology for industrial wastewater treatments as dye degradation.[29] However, several parameters as light intensity, environmental temperature, or pH of the medium can impact significantly the efficiency of the photocatalysis processes.[30] Therefore, photocatalysts should ideally gather several properties such as long-term stability under variable operational conditions, specificity towards the water pollutants, and high absorption coefficient to optimize the solar spectrum harvesting.[31]

This paper reports the enhancement effect of doping ZnO with dysprosium on the sunlight photocatalytic activity of thin films prepared using a spray pyrolysis technique. There is no previous systematic study of preparing ZnO doped Dy thin films *via* spray pyrolysis. The use of this technique shows significant advantages as compared to other methods, such as their simplicity of operation, inexpensiveness and easiness for being scaled up to mass production, leading to potential commercial applications. This paper analyzes the photocatalytic activity of the Dy doped ZnO thin films by assessing their ability to degrade methylene blue dye under natural renewable energy. The use of rare-earth doped ZnO nanomaterials for photocatalysis purposes is generally assessed by using UV or visible lamps under laboratory conditions. Nonetheless, the present work shows a degradation efficiency comparable to those already published by using natural sunlight irradiation. This fact would pave the way to degrade water pollutants as MB at industrial scale.

2. Experimental details

2.1. Preparation of undoped and Dy-doped ZnO thin films

Undoped and Dy doped ZnO thin films were deposited by chemical spray pyrolysis using an aqueous solution onto glass substrates. Before spraying the solution, the glass substrates with a dimension of 2×2 cm^2 were cleaned with a detergent, rinsed in acid, distilled water, acetone and finally dried in a furnace at 120 °C for 15 min.

The spray solution was prepared by dissolving 0.05 M zinc chloride [$ZnCl_2 \cdot 2H_2O$, Sigma Aldrich ≥% 99] in 200 ml distilled water. Whereas for the Dy doped ZnO thin films, dysprosium chloride ($DyCl_3 \cdot 2H_2O$, Sigma Aldrich) was added to the precursor solution at fixed [Dy]/[Zn] concentration ratios of 2, 4 and 6 wt%. The solution was stirred for a few minutes to obtain a homogeneous solution, then sprayed for 40 minutes through a path along the axes (x,y). The deposition temperature was fixed at 400 °C, controlled using a thermocouple related to the hot plate. The distance between the nozzle and the substrate was set to 20 cm. Compressed air was used as carrier gas at a constant flow rate of 10 ml min^{-1}, while the rate solution flow was fixed at 2 ml min^{-1}. These two parameters control the droplet size in such a way that the pyrolytic decomposition of the droplets takes place on the surface of the substrates to form thin films. Fig. 1 depicts a scheme of the spray pyrolysis method used.

2.2. Characterization of the thin films

After spraying, the study of the morphological properties and elemental compositions for the different samples was carried

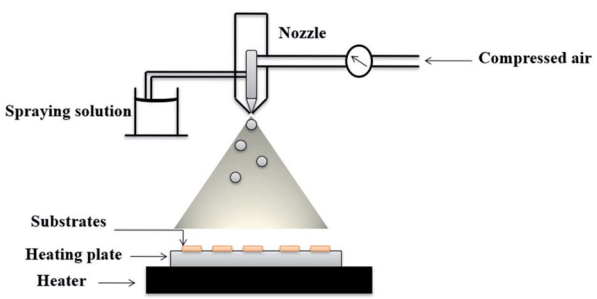

Fig. 1 Scheme of spray pyrolysis method employed.

out using electron scanning microscopy (SEM) equipped with energy dispersive spectroscopy (EDX). The measurement of the surface root mean square (RMS) roughness of the films was obtained using atomic force microscopy (AFM) (Dimension Icon, Bruker) operated in intermittent contact mode. The phase purity and the crystal structure of the samples were analysed using X-ray diffraction (XRD) (Philips X'Pert) with a copper source (Cu-Kα radiation, $\lambda = 0.154187$ Å) in the 2θ range of 20–70°.

The chemical composition of the samples and oxidation state of the ions were evaluated through X-ray photoelectron spectroscopy (XPS) using a Versaprobe PHI 219 5000 from Physical Electronics, equipped with a monochromatic 220 Al Kα X-ray source. The transmittance and reflectance measurements were carried out using a Shimadzu-UV1800 spectrophotometer in the range of 300–1800 cm. PL measurements were made using a chopped Kimmon IK Series He–Cd laser (325 nm and 40 mW). Fluorescence was dispersed with an Oriel Corner Stone 1/8 74 000 monochromator, detected using a Hamamatsu H8259-02 with a socket assembly E717-500 photomultiplier, and amplified through a Stanford Research Systems SR830 DSP.

2.3. Photocatalytic experiment

For the measurement of the photocatalytic activity, methylene blue was chosen as an organic pollutant. Its degradation under solar irradiation for different doping yields and exposure times was studied. An aqueous solution of MB with a concentration of 3 mg L^{-1} was stirred a few minutes. Afterwards, pure and Dy doped ZnO layers (2%, 4% and 6%) were placed on 4 glass boxes containing 30 ml of MB solution and were magnetically stirred and kept under dark conditions for 30 minutes. In that way, it is possible to guarantee the adsorption/desorption equilibrium between the photocatalyst and the dye. Then, they were exposed to sunlight irradiation for 2 hours, while an aliquot of 3 ml was taken every 30 min. Considering that photocatalytic experiments were conducted in Tunis (Tunisia; latitude 10.18°) using the direct sunlight, the MB photodegradation was performed under a power that is estimated to range from 180 to 230 W m^{-2}.[32]

The evaluation of the degradation of the methylene blue was studied using a Shimadzu-UV1800 spectrophotometer. This experiment was repeated three times to ensure the certainty responses of the photocatalyst. The absorption was monitored in the wavelength range of 400–900 nm, showing a decrease in the peak intensity at 660 nm. The photocatalytic degradation rate was calculated by using the following equation:[33]

$$\%\ \text{photodegradation rate} = (A_0 - A)/A_0 \quad (1)$$

where A_0 is initial absorbance of the dye solution and A is the absorbance after solar irradiation.

3. Results and discussion

3.1. Morphological analysis

Atomic force microscopy was used to evaluate the surface roughness of samples with different Dy dopant concentrations. Fig. 2 shows the two (2D) and three (3D) dimensional AFM micrographs. The images show that the surface morphology of the ZnO:Dy films are granular and consist of spherical, agglomerated, dense and compact grains. It can be observed that, the morphology does not significantly change for ZnO samples doped up to 4%.

However, a change in the morphology of the samples doped at 6% is clearly visible. At this dopant level, the particles become non-uniform and a few sharp columnar features can be observed. This can be explained by the possibility of growth and coalescence of grains during the spray pyrolysis process.[34]

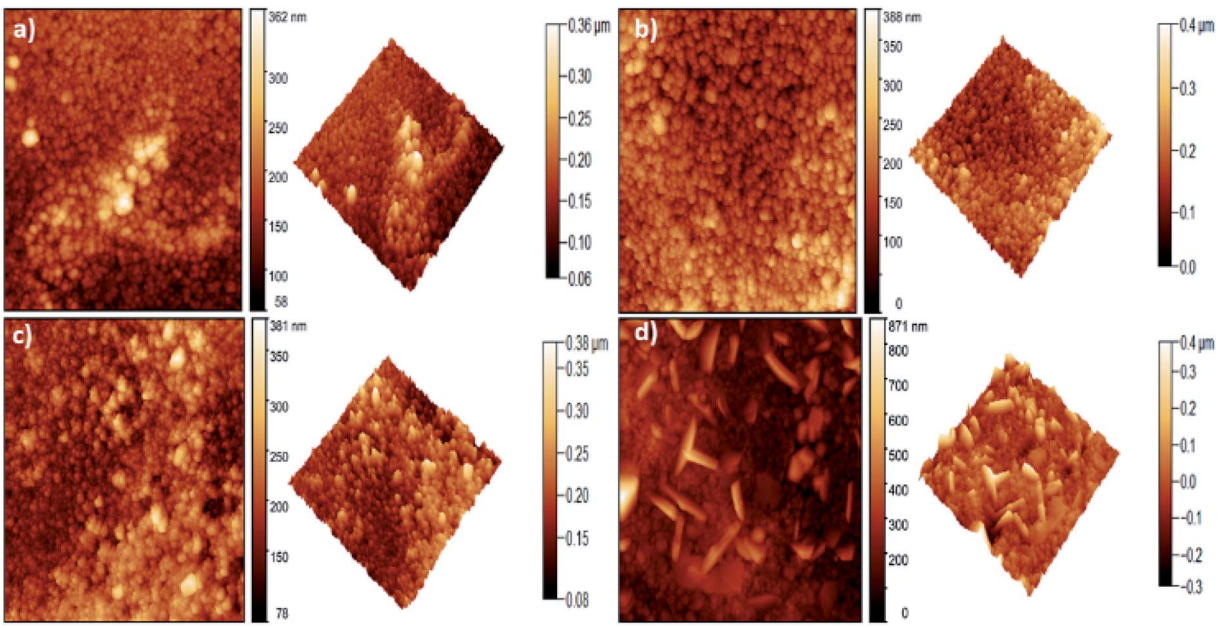

Fig. 2 2D (left side) and 3D (right side) AFM topography for (a) undoped ZnO, (b) ZnO:Dy 2%, (c) ZnO:Dy 4% and (d) ZnO:Dy 6% thin films.

Table 1 Comparison of the thin film parameters for the different samples prepared (the quantification results express the Dy wt% obtained through EDX analysis.)

Sample	Pure	Dy 2%	Dy 4%	Dy 6%
Roughness (nm)	21.66	32.38	31.68	73.08
Thickness (nm)	200	220	235	280
[Dy/Zn] (%)	0.0	1.9	4.6	6.2
E_g (eV)	3.22	3.07	3.13	2.93
E_u (meV)	509	556	680	734

Moreover, dysprosium-doping leads to an increase in the surface roughness (Table 1) from 21 nm for undoped ZnO up to 73 nm for ZnO doped at 6%. Higher roughness in thin films is one of the advantages of the spray technique. Allowing to enhance the adsorption of dye molecules at the surface, favorable for the photocatalytic degradation.

SEM images were performed for both, doped and undoped ZnO (Fig. S1, ESI†). Besides, the film thicknesses were estimated by measuring the cross-section of the SEM images. It was found that the different ZnO films were about 200–300 nm thick. Fig. 3 presents an example of the cross-section of an SEM image for a pure ZnO thin film. The value of the thickness increases as the percentage of doping increases. These results are probably related to the higher roughness registered for higher Dy content.

3.2. Structural and compositional analysis

XRD patterns of all as-deposited samples, pure and Dy^{3+} doped (2%, 4% and 6%) ZnO films are shown in Fig. 4a. All films present sharp diffraction peaks indicating a suitable crystallinity, with a preferential crystal growth along the (002) plane.

The patterns exhibited multiple peaks of pure ZnO phases with other orientations such as (100), (101), (102) and (103). These peaks correspond to the hexagonal wurtzite structure of ZnO with $P6_3mc$ space group. The indexed peaks are in agreement with the standard peak positions in JCPDS card no. 01-0.80-0074. The absence of additional peaks attributed to Dy phases indicates that Dy^{3+} ions are well incorporated into the ZnO lattice. Fig. 4b shows the 2θ angle of the main peak (002). It can be observed a small shift of this peak to higher angles with the increase of the dopant concentration, which is due to the incorporation of Dy ions into the ZnO crystal system. This could be explained by the substitution of Zn^{2+} ions having smaller ionic radii (0.74 Å) with dopant ions having higher ionic radii Dy^{3+} (0.91 Å).

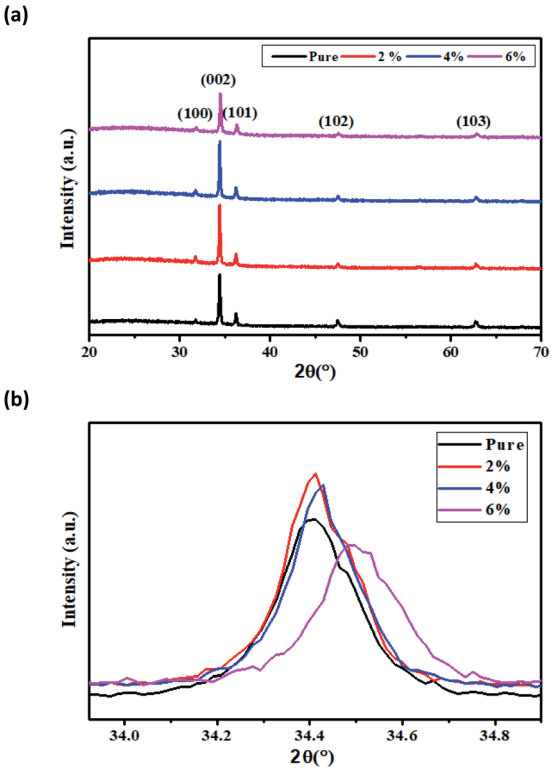

Fig. 4 (a) X-ray diffraction spectra of Dy doped ZnO thin films. (b) Shifting of the main diffraction angle with increasing doping concentrations.

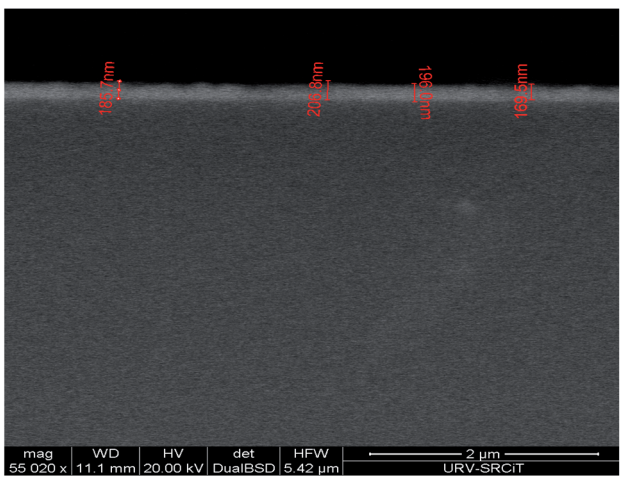

Fig. 3 Cross section of pure ZnO thin film imaged through ESEM.

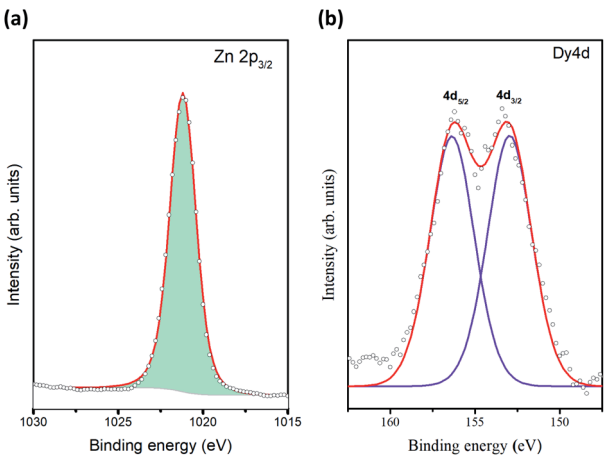

Fig. 5 The XPS spectra of (a) Zn 2p (b) Dy 4d.

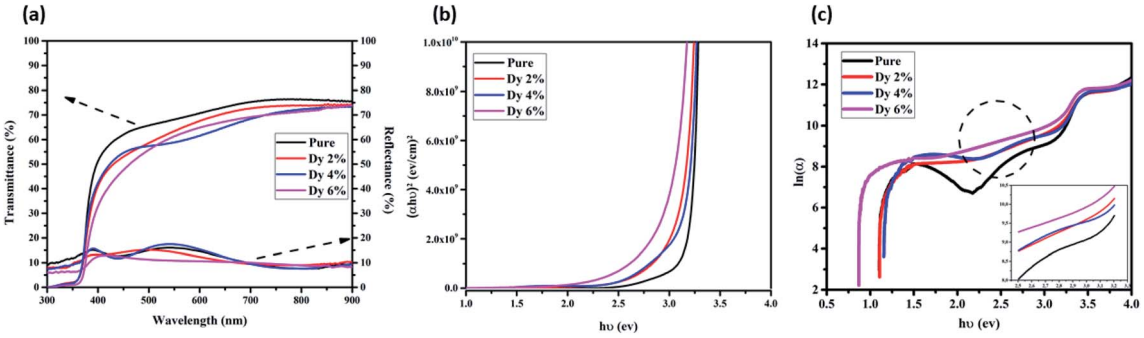

Fig. 6 (a) Optical transmittance and reflectance spectra for the Dy-doped ZnO thin films at various Dy contents. (b) Plot of $(\alpha h\nu)^2$ *versus* $(h\nu)$ of undoped and Dy-doped ZnO thin films. (c) Variation of Ln(α) with photon energy of undoped and Dy-doped ZnO thin films.

The elemental compositions of the prepared thin films were determined using the EDX, the results of the loading levels of Dy achieved in ZnO are also summarized in Table 1. These results indicate the Dy/Zn ratios achieved in the thin films, being 1.9, 4.6 and 6.2 wt%. The chemical composition of the samples was evaluated using X-ray photoelectron spectroscopy. The oxidation state of Zn and Dy ions were investigated through the analysis of the high-resolution spectra of the $Zn2p_{3/2}$, Zn LMM and Dy4d core levels. The Zn LMM Auger data (Fig. 5a) shows the fingerprint for Zn^{2+} oxidation state,[35] this assertion is validated by the observation of the $Zn2p_{3/2}$ peak centered at 1021.1 eV corresponding to Zn^{2+}. The XPS spectrum recorded in the region of the Dy4d core level (Fig. 5b) shows a doublet with components centered at 153.2 eV ($Dy4d_{3/2}$) and at 156.6 eV ($Dy4d_{5/2}$), these components denote the presence of Dy^{3+},[36] and no other oxidation state was founded. Table S2 (ESI†) depicts the comparison of pure ZnO and 6% Dy doped quantification through XPS. Indeed, O 1s core level was also analyzed for both, pure ZnO and Dy doped (Fig. S2, ESI†). Two main peaks were observed at 530.0 eV and 531.8 eV, attributed to lattice oxygen of Zn–O and Zn–OH groups (defective ZnO), respectively.[37,38]

Experimental results of XPS are in agreement with XRD, confirming that Dy^{3+} is incorporated into the ZnO lattice as a substitutional dopant and compensating the charges. Besides, Zn vacancies are formed.[39,40]

3.3. Optical analysis

The transmittance and reflectance spectra of the pure and Dy-doped ZnO thin films are shown in Fig. 6a. These films show high transparency within the visible range and near the IR region with an average transmittance varying between 75% and 85% and a sharp fundamental absorption edge in the UV region. The overall average reflectance values are about 15%. The high transparency of these samples would enable their use as an optical window in solar cell applications.

In addition, the optical absorption edge of Dy-doped ZnO films is red-shifted compared to pure samples, moving forward to the visible light region. This red-shift may be due to the formation of shallow electronic levels inside the bandgap occurring from the doping atoms residing in the lattice.[41]

The direct bandgap energy (E_g) of ZnO thin films semiconductors is the transition between the valence and conduction bands, obtained by extrapolating the linear portion of the plots of $(\alpha h\nu)^2$ *versus* $h\nu$ to $h\nu = 0$. It can be calculated using the Tauc model[42] as indicated in the following equation:

$$(\alpha h\nu)^2 = B(h\nu - E_g) \quad (2)$$

$$\alpha = \frac{1}{d}\left(\frac{(1-R)^2}{T}\right) \quad (3)$$

where ν is the frequency of the incident photon, $h\nu$ is photon energy, B is a constant and α is the absorption coefficient, α is the absorption coefficient and d is the thickness of the sample considered.[43]

Fig. 6b shows the optical bandgap energy for the undoped and doped samples. The bandgap decreases from 3.22 eV to 2.93 eV when the Dy doping level increases. This shift of the energy gap can be explained by the generation of defects and disorder in the ZnO lattice due to the incorporation of dopants, which influences the structure of the bandgap, thus allowing the formation of localized states and deep levels in the bandgap. Similar results were reported by O. Yayapao *et al.*,[41] revealing a decrease in the bandgap following the introduction of Dy ions in the ZnO matrix. Indeed, the decrease in the band gap energy facilitates the increase in the separation of the photo-induced electron–hole pairs, resulting in an easier electron excitation.

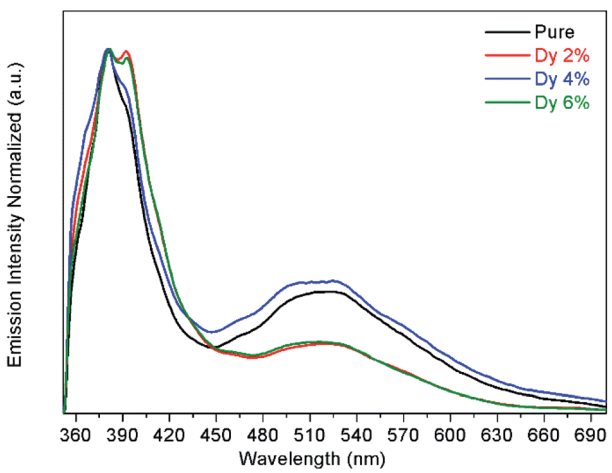

Fig. 7 PL spectra for the Dy-doped ZnO thin films at various Dy contents.

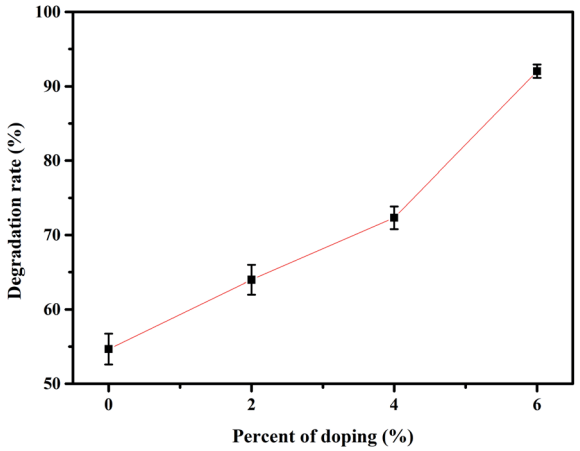

Fig. 8 Degradation rate of MB after solar irradiation for 2 hours using the Dy doped ZnO thin films at various Dy contents.

These results enhance the visible light photocatalytic efficiency of the Dy-doped ZnO.[44]

The Urbach energy gives an idea about the disorder in the samples and can be calculated using the Urbach law (see Fig. 6c):[45]

$$\alpha = \alpha_0 \exp\left(\frac{h\nu}{E_u}\right) \quad (4)$$

where α is the absorption coefficient, α_0 is a constant, $h\nu$ is the incident photon energy. The reverse of the slope of the plot Ln(α) *versus* $h\nu$ gives the value of the E_u. Table 1 also presents the dependence of Urbach energy on Dy amount. The Urbach energy increases from 509 meV to 734 meV by doping with Dy, which is indicative of the increasing disorder in the films with the increase in the doping level. The increase in the Urbach energy values with the increase in the Dy doping concentration indicates that the density of defects increases in the bandgap structure of the thin films doped with Dy. In fact, according to the optical results, it can be assumed that Dy atoms were successfully incorporated to the ZnO lattice and the decrease in the bandgap width observed in Dy-doped samples enhances the absorption of solar energy in the visible range.

The PL spectroscopy is employed to investigate the separation capacity of the electron–hole pairs and to probe the crystal defects because it originates from either the photoinduced electron–hole bandgap recombination or in the intrinsic defects. Fig. 7 shows the PL spectra for the undoped and doped samples. By pumping at 325 nm, it can be observed two emission bands, one emission in the UV at around 380 nm and a broader emission band in the visible range from 450 to 700 nm. The UV peak corresponds to the near band-edge emission, associated with exciton recombination processes,[46] while the broad emission band observed in the visible range is attributed to defects.[47]

The exciton peak is located at 380 nm for the undoped and 2, 4% doped samples, while for the 6% doped sample is shifted to 382 nm. Also, another peak is observed at 393 nm for the doped samples. This second peak can be explained by the formation of a shallow level inside the band gap and close to the conduction band of ZnO, and is due to the impurity Dy^{3+} atoms substituting the Zn^{2+} atoms in the lattice, which is was also corroborated by the red-shift observed in the transmittance and reflectance spectra results. The full width at half maximum (FWHM) of this UV peak increases from 387 to 477 meV from the undoped to the 6% doped sample. This broadening observed on the FWHM indicates that the recombination of photogenerated electron–hole pairs increases as the Dy-doping increases. On the other hand, the defect band has its maximum emission intensity at around 520 nm and could be related to oxygen vacancies.[47] This PL results are in agreement with the transmittance and reflectance measurements.

3.4. Photocatalytic activity

The photocatalytic activity of the undoped and Dy doped ZnO thin films was evaluated using methylene blue (MB). Since this organic dye shows a strong absorbance band at 660 nm, their intensity decreases when MB degrades, this variation in the intensity was assessed at regular time intervals.

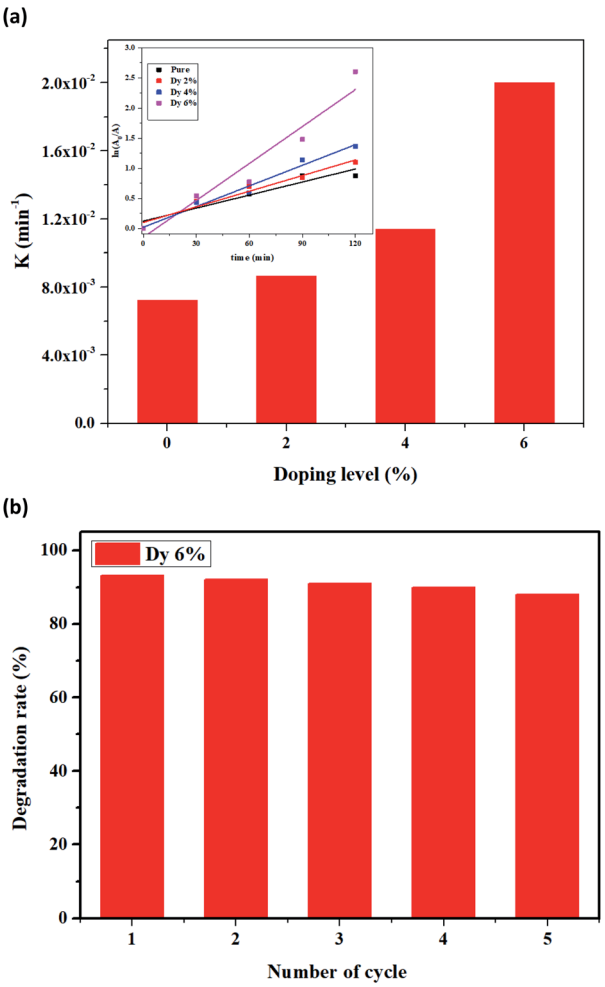

Fig. 9 (a) The kinetic rate K as a function of Dy content. (b) Recyclability of Dy doped ZnO at 6%.

The time evolution of absorbance spectra for pure and ZnO doped thin films (2%, 4% and 6%), recorded from 400–900 nm wavelengths for MB dye solutions irradiated under solar irradiation (Fig. S3, ESI†). These figures show that, as time elapses, the intensity of the peak at 660 nm decreases revealing that the MB is rapidly degrading. For a given period elapsed, as the Dy doping of ZnO increases the difference between the intensity of the 660 nm peak is also increased. This indicates that 6% Dy doped ZnO is the most efficient at degrading MB irradiation time. The MB degradation rate (calculated using eqn (1)) for all the samples tested after 120 minutes under solar irradiation. Indeed, the photocatalytic efficiency increases with doping content and the highest value of about 92% was characteristic of the sample doped at 6% under sunlight irradiation (Fig. 8). The obtained results are in good agreement with those found by S. Nguanprang *et al.* for Dy-doped ZnO nanoparticles at 5% deposited by the combustion technique.[48] This increase in photocatalytic activity with the increase in doping can be explained by the inhibition of the recombination of photogenerated electron–hole pairs following the substitution of Zn^{2+} by Dy^{3+}. Indeed, the optical and morphological results confirm this enhancement, and the sample doped at 6% with Dy presents the lowest value of bandgap energy. Besides, this sample shows the highest surface roughness (RMS), leading to an increase in the adsorption of the MB on the surface.

This parameter facilitates the separation and the transfer of photogenerated charge carriers, resulting in an enhancement of photocatalytic efficiency.[49]

The kinetic rate K can be calculated using the following equation:[50]

$$\ln(A_0/A) = Kt \quad (5)$$

where A_0 is the initial absorbance of the MB dye, A is the absorbance of the MB dye after irradiation time 't' and K is pseudo first-order rate constant. The variation between degradation ratios $\ln(A/A_0)$ of MB dye and time for the pure and Dy-doped ZnO was examined and is represented in the inset in Fig. 9a. The constant rate K is determined from the slope of the $\ln(A/A_0)$ *versus* irradiation time (t) plot (Fig. 9a). It can be deduced from the figures that the value of the reaction rate constant increases when the doping concentration increases, which proves that the doping of ZnO with Dy enhances the photocatalytic performance under solar light. The 6% Dy-doped ZnO thin films achieved the highest reaction rate, being comparable to those that use lamps under laboratory conditions. (Table S3, ESI†) depicts a comparison of the photocatalytic activities obtained for ZnO samples doped with rare-earth materials when degrading dyes. It is worth noting that the highest Dy content (6%) showed the best photodegradation rate. Thereby, it cannot be ruled out that further increases in the dopant concentration might improve the efficiency of the photocatalytic process to some extent. However, since the dopant induces distortions into the ZnO lattice, an optimum dopant level should exist that results in the highest dye degradation rate.

In order to study the stability of the degradation efficiency for the 6% Dy-doped ZnO sample, five consecutive cycles of MB degradation under solar light were performed (Fig. 9b). A cleaning protocol of the surface was used before each cycle to ensure a reliable film recovery. Specifically, the active layer was rinsed several times with distilled water and dried with nitrogen. Finally, a thermal treatment was conducted in a oven for 15 min at 200 °C. As a result, a negligible decrease in the photocatalytic efficiency was observed after five cycles, demonstrating the outstanding stability of Dy doped ZnO thin films for degrading methylene blue. It is worth noting that ZnO is prone to suffering photo-corrosion than other materials such as TiO_2,[51] however, with the experimental conditions applied, a noteworthy recyclability of the thin films developed was achieved.

3.5. Mechanism of photocatalytic degradation

The proposed degradation mechanism of MB in the presence of a Dy-doped ZnO thin film is described in detail. It is well-known that hydroxyl radicals remove the organic contaminants from wastewater on the surface of the Dy-doped ZnO thin films. Whereas, when the energy of the incident light is equal or exceeds the bandgap energy, thin films generate at the surface electron/hole (e^-/h+) pairs. The mechanism is presented in the steps below:

$$ZnO + h\nu \rightarrow h^+_{vB} + e^-_{CB} \quad (6)$$

The production of holes under solar irradiation by the oxygen vacancies:

$$V^+oxg + e^- \rightarrow Voxg + h^+_{vB} \quad (7)$$

The reaction between ($h_{VB}{}^+$) with the adsorbed water (H_2O) at the surface of the thin films produces hydroxyl radicals ($OH^\bullet$)

$$ZnO + h^+_{vB} + H_2O(ads) \rightarrow H^+ + OH^\bullet \quad (8)$$

In addition, dysprosium is a powerful Lewis acid with a partly occupied 4f orbital can easily react with electrons from the conduction band. Consequently, Dy can trap electrons *via* the conduction band and thus, enhance the inhibition of the recombination of charge carriers.[52]

$$Dy^{3+} + e^-_{CB} \rightarrow Dy^{2+} \quad (9)$$

$$Dy^{2+} + O_2(ads) \rightarrow O_2{}^{\bullet -} \quad (10)$$

$$O_2{}^{\bullet -} + H^+ \rightarrow HO_2{}^\bullet \quad (11)$$

In fact, water molecules and oxygen permit to trap the holes and electrons to form hydroxyl radicals that react with the dye molecule present in the solution, favoring its degradation.

$$HO_2{}^\bullet + H^+ + e^-_{CB} \rightarrow H_2O_2 \quad (12)$$

$$H_2O_2 + e^-_{CB} \rightarrow HO^\bullet + OH^- \quad (13)$$

$$h^+_{vB} + H_2O \rightarrow H^+ + OH^\bullet \quad (14)$$

$$H^+ + OH^\bullet \rightarrow HO^\bullet \text{ (formation of hydroxyl radical)} \quad (15)$$

Hydroxyl radicals $OH^{\bullet}$ enable the decomposition of hazardous pollutants as MB into inorganic compounds, which makes the solution colorless.

(Mineralization of MB dye)

$$\text{MB dye} + OH^{\bullet} \rightarrow CO_2\uparrow + H_2O \quad (16)$$

Thereby, the complete decomposition of MB results in CO_2 and H_2O. However, it can be expected that intermediate compounds are formed during the photodegradation process. For instance, gas-chromatography-mass spectrometry analyses have revealed the presence of benzoic acid groups during the photodegradation process of MB.[53,54] It is worth noting that photodegradation of MB was performed under scavenger-free conditions, which is leading to optimum decomposition rates. For instance, U. Alam *et al.* studied the role of different scavengers in MB degradation using Nd-ZnO nanoparticles.[55] Specifically, this work reports the use of isopropyl alcohol, benzoquinone and EDTA-2Na to trap $OH^{\bullet}$, $O_2^{\bullet-}$ and holes. As a result of this scavenger-assisted process, the highest reduction in the MB degradation rate was achieved using isopropyl alcohol, due to the quenching of hydroxyl radicals, revealing their key importance during the photocatalytic process.

4. Conclusions

We have investigated the structural, optical and morphological properties of pure and dysprosium doped ZnO thin films prepared by a simple chemical method of spray pyrolysis. XRD measurements proved the presence of the hexagonal wurtzite phase of ZnO and no additional peaks wer introduced by doping with dysprosium elements. The obtained AFM images showed an increase in the roughness of the ZnO thin films by Dy doping until 73 nm at 6%. XPS results confirm that in doped ZnO, Dy^{3+} is incorporated into the ZnO lattice. The transmittance spectra show that all films have a transmittance in the range of 80% in the visible range and the optical bandgap decreases from 3.22 eV in undoped samples to 2.93 eV for samples doped with 6% Dy favoring the degradation of MB under solar irradiation.

The dye degradation in the presence of pure ZnO was found to be 57% and increased up to 92% for Dy doped ZnO at 6%. This is the highest efficiency achieved throughout the samples tested. With that, Dy-doped ZnO thin films have a great potential to be employed in photocatalytic applications for wastewater purification.

Conflicts of interest

There are no conflicts to declare.

Acknowledgements

E. L. is supported by the Catalan Institution for Advanced Studied *via* the 2018 Edition of the ICREA Academia Award. CB is a Research Associate of the National Funds for Scientific Research (FNRS, Belgium). This work was supported in part by MICINN and FEDER *via* grants no. RTI2018-101580-B-I00.

References

1 L. Diamandescu, M. Cernea, F. Tolea, E. C. Secu, R. Trusca, M. Secu and M. Enculescu, *Ceram. Int.*, 2018, **44**, 21962–21975.
2 D. P. Ojha and H. J. Kim, *Chem. Eng. Sci.*, 2020, **212**, 115338.
3 S. Rehman, R. Ullah, A. M. Butt and N. D. Gohar, *J. Hazard. Mater.*, 2009, **170**, 560–569.
4 S. Fatin, H. N. Lim, W. T. Tan and N. M. Huang, *Int. J. Electrochem. Sci.*, 2012, **7**, 9074–9084.
5 R. E. Adam, H. Alnoor, G. Pozina, X. Liu, M. Willander and O. Nur, *Solid State Sci.*, 2020, **99**, 106053.
6 M. Willander, M. Q. Israr, J. R. Sadaf and O. Nur, *Nanophotonics*, 2012, **1**, 99–115.
7 A. Mhamdi, M. S. Alkhalifah, S. Rajeh, A. Labidi, M. Amlouk and S. Belgacem, *Phys. B*, 2017, **521**, 178–187.
8 M. Wang, Y. Lian and X. Wang, *Curr. Appl.*, 2009, **9**, 189–194.
9 D. Raoufi, *J. Lumin.*, 2013, **134**, 213–219.
10 L. Zhu and W. Zeng, *Sens. Actuators, A*, 2017, **267**, 242–261.
11 S. Bhatia, N. Verma and R. Kumar, *J. Alloys Compd.*, 2017, **726**, 1274–1285.
12 A. Hastir, N. Kohli and R. C. Singh, *J. Phys. Chem. Solids*, 2017, **105**, 23–34.
13 S. P. Chand and V. Singh, *J. Rare Earths*, 2020, **38**, 29–38.
14 S. Selvaraj, M. K. Mohan, M. Navaneethan, S. Ponnusamy and C. Muthamizhchelvan, *Mater. Sci. Semicond. Process.*, 2019, **103**, 104622.
15 L. Yang, Y. Tang, A. Hu, X. Chen, K. Liang and L. Zhang, *Phys. B*, 2008, **403**, 2230–2234.
16 A. George, S. K. Sharma, S. Chawla, M. M. Malik and M. S. Qureshi, *J. Alloys Compd.*, 2011, **509**, 5942–5946.
17 A. N. Ökte, *Appl. Catal., A*, 2014, **475**, 27–39.
18 G. A. S. Josephine and A. Sivasamy, *Appl. Catal., B*, 2014, **150–151**, 288–297.
19 L. Xu, G. Zheng, F. Xian and J. Su, *Mater. Chem. Phys.*, 2019, **229**, 215–225.
20 M. Yarahmadi, H. Maleki-Ghaleh, M. E. Mehr, Z. Dargahi, F. Rasouli and M. H. Siadati, *J. Alloys Compd.*, 2021, **853**, 157000.
21 L. Roza, Y. Febrianti, S. Iwan and V. Fauzia, *Surf. Interfaces*, 2020, **18**, 100435.
22 H. Jafari, S. Sadeghzadeh, M. Rabbani and R. Rahimi, *Ceram. Int.*, 2018, **44**, 20170–20177.
23 G. Poongodi, R. M. Kumar and R. Jayavel, *Ceram. Int.*, 2015, **41**, 4169–4175.
24 W.-H. Lin, Y.-H. Chiu, P.-W. Shao and Y.-J. Hsu, *ACS Appl. Mater. Interfaces*, 2016, **8**, 32754–32763.
25 Y.-C. Pu, H.-Y. Chou, W.-S. Kuo, K.-H. Wei and Y.-J. Hsu, *Appl. Catal., B*, 2017, **204**, 21–32.
26 C. Florica, A. Costas, N. Preda, M. Beregoi, A. Kuncser, N. Apostol, C. Popa, G. Socol, V. Diculescu and I. Enculescu, *Sci. Rep.*, 2019, **9**, 17268.
27 Y.-C. Chen, T.-C. Liu and Y.-J. Hsu, *ACS Appl. Mater. Interfaces*, 2015, **7**, 1616–1623.
28 T. A. Kurniawan, Z. Mengting, D. Fu, S. K. Yeap, M. H. D. Othman, R. Avtar and T. Ouyang, *J. Environ. Manage.*, 2020, **270**, 11087.

29 Y.-A. Chen, Y.-T. Wang, H. S. Moon, K. Yong and Y.-J. Hsu, *RSC Adv.*, 2021, **11**, 12288–12305.
30 Y.-H. Chiu, T.-F. Chang, C.-Y. Chen, M. Sone and Y.-J. Hsu, *Catalysts*, 2019, **9**, 430.
31 M.-J. Fang, C.-W. Tsao and Y.-J. Hsu, *J. Phys. D: Appl. Phys.*, 2020, **53**, 143001.
32 K. Belkilani, A. B. Othman and M. Besbes, *Appl. Phys. A*, 2018, **124**, 122.
33 R. Nasser, W. B. H. Othmen, H. Elhouichet and M. Férid, *Appl. Surf. Sci.*, 2017, **393**, 486–495.
34 M. A. Amara, T. Larbi, A. Labidi, M. Karyaoui, B. Ouni and M. Amlouk, *Mater. Res. Bull.*, 2016, **75**, 217–223.
35 J. O. Primo, C. Bittencourt, S. Acosta, A. Sierra-Castillo, J.-F. Colomer, S. Jaerger, V. C. Teixeira and F. J. Anaissi, *Front. Chem.*, 2020, **8**, 11.
36 X. Dong, X. Cheng, X. Zhang, L. Sui, Y. Xu, S. Gao, H. Zhao and L. Huo, *Sens. Actuators, B*, 2018, **255**, 1308–1315.
37 M. Kumar, G. Josephine, G. Tamilarasan, A. Sivasamy and J. Sridevi, *J. Environ. Chem. Eng.*, 2018, **6**, 3907–3917.
38 A. Fonseca, R. Siqueira, R. Landers, J. L. Ferrari, N. L. Marana, J. R. Sambrano, F. A. L. Porta and M. A. Schiavon, *J. Alloys Compd.*, 2018, **739**, 939–947.
39 M. Prathap Kumar, G. A. Suganya Josephine, G. Tamilarasan, A. Sivasamy and J. Sridevi, *J. Environ. Chem. Eng.*, 2018, **6**, 3907–3917.
40 F.-Y. Lo, Y.-C. Ting, K.-C. Chou, T.-C. Hsieh, C.-W. Ye, Y.-Y. Hsu, M.-Y. Chern and H.-L. Liu, *J. Appl. Phys.*, 2015, **117**, 213911.
41 O. Yayapao, T. Thongtem, A. Phuruangrat and S. Thongtem, *J. Alloys Compd.*, 2013, **576**, 72–79.
42 J. Tauc, R. Grigorovici and A. Vancu, *Phys. Status Solidi B*, 1966, **15**, 627–637.
43 D. E. Milovzorov, A. M. Ali, T. Inokuma, Y. Kurata, T. Suzuki and S. Hasegawa, *Thin Solid Films*, 2001, **382**, 47–55.
44 R. Mimouni, A. Souissi, A. Madouri, K. Boubaker and M. Amlouk, *Curr. Appl. Phys.*, 2017, **17**, 1058–1065.
45 Y. Zhang, Y. Shen, F. Gu, M. Wu, Y. Xie and J. Zhang, *Appl. Surf. Sci.*, 2009, **256**, 85–89.
46 J. S. Reparaz, F. Güell, M. R. Wagner, G. Callsen, R. Kirste, S. Claramunt, J. R. Morante and A. Hoffmann, *Appl. Phys. Lett.*, 2010, **97**, 133116.
47 F. Güell and P. R. Martínez-Alanis, *J. Lumin.*, 2019, **210**, 128–134.
48 S. Sa-nguanprang, A. Phuruangrat, T. Thongtem and S. Thongtem, *Inorg. Chem. Commun.*, 2020, **117**, 107944.
49 J. Yin, Z. Xing, J. Kuang, Z. Li, M. Li, J. Jiang, S. Tan, Q. Zhu and W. Zhou, *J. Alloys Compd.*, 2018, **750**, 659–668.
50 J.-C. Sin, S.-M. Lam, K.-T. Lee and A. R. Mohamed, *Ceram. Int.*, 2014, **40**, 5431–5440.
51 X.-B. Xiang, Y. Yu, W. Wen and J.-M. Wu, *New J. Chem.*, 2018, **42**, 265–271.
52 J.-C. Sin, S.-M. Lam, K.-T. Lee and A. R. Mohamed, *Ceram. Int.*, 2013, **39**, 5833–5843.
53 B. Yang, J. Zuo, X. Tang, F. Liu, X. Lu, X. Tang, H. Jiang and L. Gan, *Ultrason. Sonochem.*, 2014, **21**, 1310–1317.
54 J. Lin, X. Weng, X. Jin, M. Megharaj, R. Naidu and Z. Chen, *RSC Adv.*, 2015, **5**, 70874–70882.
55 U. Alam, A. Khan, D. Ali, D. Bahnemann and M. Muneer, *RSC Adv.*, 2018, **8**, 17582–17594.